Binary CoOx-SiO 2 Porous Nanostructures for Catalytic CO Oxidation

Isabelle Ly, Antoine Vardon, Nicolas Chanut, Frédéric Nallet, Rolland J Pellenq, Mathieu Rouzières, Rodolphe Clérac, Joudia Akil, Florence Epron, Catherine Especel, et al.

Binary CoOx-SiO_2 Porous Nanostructures for Catalytic CO Oxidation

Isabelle Ly,[1] Antoine Vardon,[1] Nicolas Chanut,[2] Frédéric Nallet,[1] Rolland J. Pellenq,[2] Mathieu Rouzières,[1] Rodolphe Clérac,[1] Joudia Akil,[3] Florence Epron,[3] Catherine Especel[3,*] and Rénal Backov[1,*]

[1] Université de Bordeaux, CRPP-UMR CNRS 5031, 115 Avenue Albert Schweitzer, 33600 Pessac, France.

[2] Massachusetts Institute of Technology, Department of Civil and Environmental Engineering, 77, Mass. Avenue, Cambridge MA 02139, USA.

[3] Institut de Chimie des Milieux et Matériaux de Poitiers (IC2MP), UMR 7285 CNRS - Université de Poitiers, 4 rue Michel Brunet, TSA 51106, 86073 Poitiers Cedex 9 – France.

* Corresponding authors: renal.backov@crpp.cnrs.fr, catherine.especel@univ-poitiers.fr

Abstract

Through the integration of sol-gel chemistry, lyotrope mesophases and emulsions, the first CoOx-SiO_2(HIPE) series of cobalt nano-oxides were embedded within silica macro-mesocellular self-standing hosts. These binary CoOx-SiO_2 porous nanostructures (MUB-100(x)) series present an average of 95% porosity. We found out that high cobalt concentration maintains the hexagonal-2D organization of the mesoscopic voids when applying the thermal treatment at 700°C. Their specific surface areas fall between 400-500 m^2 g^{-1} when assessed from Ar physi-sorption measurements. At the microscopic length scale, as revealed through magnetic investigations, the low cobalt content foams MUB-100(1) and MUB-100(2) are made of the amorphous β-$Co(OH)_2$ phase coexisting with the silica network, while increasing the cobalt concentration during the one pot syntheses (MUB-100(3) and MUB-(4) materials) favors the formation of the spinel Co_3O_4 and olivine Co_2SiO_4 crystalline nanoparticles embedded within silica. When it turns towards the CO oxidation catalytic performance, the MUB-100(4) is able to totally convert the CO flow before 200°C (starting at 125°C) while achieving 50% of conversion for a light-off temperature T_{50} of 145°C, revealing the good efficiency of the MUB-100(4) in CO oxidation with which up to 4 catalytic cycles have been performed without disrupting drastically the catalytic performances while reaching thermodynamic stability from the cycle 2 to the cycle 4.

KEYWORDS: sol-gel process, hierarchical porous materials, CO oxidation, integrative chemistry, heterogeneous catalysis

1. INTRODUCTION

Polymerization/polycondensation of emulsion continuous phases and removal of the dispersed one used as a soft template, lead to solid microcellular foams. Various synthetic routes of these systems have been reviewed by M. S. Silverstein *et al.*[1,2], while providing for instance a complete "contemporary contemplation" of the domain. The network precursors being organic can be varied on demand offering thus a real "*holy grail*"[3] when it turns solely towards organic poly(HIPE), H.I.P.E. being the acronym for High Internal Phase Emulsion.[4] When looking at inorganic porous media, this synthetic path is making the use of a synergistic templating effects combining (i) lyotrope mesophases (concentrated micelles), which create the mesoporosity (pore diameters ranging from 2 to 50 nm), (ii) concentrated oil-in-water emulsions (direct emulsions) inducing the connected macroporosity (pore diameters above 50 nm), and (iii) the sol-gel process that condenses the continuous hydrophilic phase.[5] As the inorganic skeleton is made of amorphous silica, the microporosity (pore diameters below 2 nm) relies on the statistical repartition of SiO_4 tetrahedrons within the geometrical space. These self-standing foams are labelled Si(HIPE),[5] and they can be further hybridized for applications towards heterogeneous catalysis.[6-9] For example, when considering inorganic mix of titania and silica, porous materials have been recently designed and employed within the fields of random lasing[10-12] or towards CO_2 photoreduction in volume.[13] Aside, we were also able to associate silica and alumina inducing highly efficient acidic heterogeneous catalysts.[14] Despite these results, there is still a lack of research dedicated to inorganic-HIPE when comparing with the field of organic polyHIPE. This reduced endeavor is emerging from the inorganic synthetic path tendency to shrink the inorganic skeleton through both intrinsic polycondensation and applied thermal treatment. Additionally, drying the monolith has to

hamper capillarity forces. As such, obtaining inorganic self-standing monolithic materials is not such an easy task to achieve. Despite this drawback, we have recently generated SBA15-Si(HIPE) materials being both 2D-hexagonal mesoporous and monolithic while leveraging a chaotrope-kosmotrope salt effect.[15,16] Aside, there are also strong research efforts to generate novel mixed-nano-oxides-inorganic-foams from the HIPE process considering the full Mendeleïev table as, like ceramics, they are resilient both to solvent and temperature while maintaining high surface area when addressing the nanoscale. They are thus outstanding candidates for liquid or gaseous phase heterogeneous catalysis. Particularly, the heterogeneous oxidation of CO is currently the most effective gas exhaust remediation approach where most of the commercial catalysts are making use of noble metals, due to their high activity for CO oxidation and stability.[17–23] However, it is well-known that the major drawbacks of noble metals are their scarcity and associated highly increasing cost.[17,24] Consequently, several studies have been reported on the development of non-noble transition metal-based catalysts for CO oxidation,[17,25–30] where cobalt oxides, Co_3O_4 especially, represent promising candidates.[17,31] In this vein, we are proposing the design of the first CoOx-SiO_2(HIPE) macro-mesocellular monolith MUB-100 series (MUB being the acronym for "Materials of the University of Bordeaux"), their characterization and specific applications as highly efficient heterogeneous catalysts towards CO oxidation.

2. EXPERIMENTAL SECTION

2.1 Material syntheses. High purity dodecane (≥ 99%), hydrochloric acid 37wt % (HCl), tetraethylorthosilicate (≥ 99%, TEOS) and cobalt (II) chloride hexahydrate $CoCl_2$. $6H_2O$ were purchased from Sigma-Aldrich. Tetradecyltrimethylammonium bromide (TTAB) was supplied by Alfa Aesar, while dichloromethane (CH_2Cl_2, ACS-reagent RPE) was purchased from Carlo Erba. All the chemicals were used as received without any further purification. Deionized water was obtained using a Milli-Q water purification system. $CoCl_2.6H_2O$

(3.255, 1.713, 0.571 or 0.2852 g) were dissolved in 16 g of a TTAB (35wt %) water solution. Then 5 g of HCl (37wt %) were added prior adding 5 g of TEOS (pH 0.05). The solution was let under stirring 10 minutes both to promote TEOS full hydrolysis and allow partial evaporation of the native ethanol. Then, 37 g of dodecane were emulsified drop by drop into a mortar through a manual stirring. The native direct oil-in-water emulsion was then transferred into several hemolysis test tubes employed as canisters, where the sol-gel process is let to proceed during one week at 25°C. Then the solidified emulsions were pulled out of the canister and let to wash for 12 hours in dichloromethane (CH_2Cl_2). The wet materials were let to dry in a desiccator for one week and further in air during three days. Finally, a thermal treatment was applied to the materials in order to sinter the silica network, calcine the TTAB surfactant employed as a mesoscopic mold, and promote the cobalt oxide nucleation and growth. The thermal treatment was applied under atmospheric conditions as follow: a first temperature increase was applied at 2°C/min until 180°C with a 6 hours' plateau followed by a second temperature ramp at 1°C/min to reach 700°C with a 6 hours' plateau. The cooling process was uncontrolled and directed by the oven inertia. Final expected micro-meso-macroporous self-standing monoliths are labeled MUB-100(1), MUB-100(2), MUB-100(3) and MUB-100(4) while increasing the amount of cobalt employed for the syntheses (Table 1). Final materials are shown on Figure 1.

2.2 Material Characterizations.

2.21. Scanning Electron Microscopy (SEM). The sample was properly broken down and stuck on an aluminum holder and glue with silver paint. Then the fractured surface was metalized with gold / palladium sputtering. SEM images were acquired with a Hitachi TM-1000 tabletop scanning electron microscope operating with at 15 kV accelerating voltage. The Energy-Dispersive X-ray Spectroscopy (EDS) spectra and the mappings were obtained on a ZEISS EVO 50 scanning electron microscope equipped with an EDX EDAX detector. The

electronic source was a lanthanum hexaboride tip (LaB_6) and the accelerating voltage was 20 kV.

2.22. X-Ray diffractions. X-ray diffraction (XRD) patterns were collected on a PANalitycal X'pert MPD-PRO Bragg-Brentano θ-θ geometry diffractometer equipped with a secondary monochromator and an X'celerator detector over an angular range of 2θ = 8-80°. Each acquisition lasted for 6h47. The Cu-Kα radiation was generated at 45 kV and 40 mA (lambda = 0.15418 nm). The samples were prepared on silicon wafer "zero background" sample holder and flattened with a piece of glass.

2.23. Small-Angle X-ray Scattering (SAXS). X-ray diffraction experiments were performed on an XEUSS 2.0 device (XENOCS) with a microfocus copper anode source. Coupled to a FOX3D XENOCS single reflection optical mirror centered on the Cu Kα radiation (λ = 1.54 Å), the system delivers a 8 keV beam which is collimated and defined by a set of 2 motorized scatterless slits. The samples were put in thin glass capillaries and exposed 2 hours. The data were collected by a two-dimensional DECTRIS PILATUS-300k detector placed at a distance of 1190 mm giving access to a range of scattering wave vectors q between 0.007 and 0.2 A^{-1}. The diffractograms of the diffracted intensity *I vs q* are obtained by processing the images with the software "FOXTROT" resulting from a collaboration between XENOCS and the teams of the synchrotron "SOLEIL".

2.24. Transmission Electron Microscopy (TEM) – Transmission Electron Diffraction (TED). The samples were ground in a mortar then dissolved in ethanol. A drop of the solution was placed and dried on a TEM copper grid covered with a carbon film. The TEM pictures were obtained with a transmission electron microscope Hitachi H7650 operating at 80 kV while the diffraction patterns were generated with a TEM FEI Talos™ F200S 200 kV. Regarding the coupled TEM-TED investigations, images and electron diffraction patterns were collected on a JEOL 2100 transmission electron microscope, working at 200 kV and

equipped with a double tilt specimen stage. Prior to its observation, a suspension of the specimen in alcohol was prepared and a drop was deposited on a carbon coated grid.

2.25. Magnetism measurements. The magnetic susceptibility measurements were performed using a PPMS-Evercool II Quantum Design magnetometer with a VSM module operating between 1.9 and 300 K for applied dc fields ranging from −9 T to 9 T. Measurements were done on ground samples (12.63, 8.17, 9.41 and 8.33 mg for MUB-100(1), MUB-100(2), MUB-100(3) and MUB-100(4), respectively), which were loaded into a sealed polyethylene bag (typically 25 mg). For MUB-100(1), MUB-100(2), MUB-100(3) and MUB-100(4), the field dependence of the magnetization was measured at 100 K, to verify the absence of significant ferromagnetic impurities. The magnetic susceptibility was measured in the range 2 – 300 K range at 0.1 T. Field dependence of the magnetization up to 9 T was measured at 2, 3, 5 and 8 K, and a complete hysteresis loop done at 2 K (at 0.2 T/min). Zero-Field-Cooled (ZFC) - Field-Cooled (FC) experiments were done between 2 and 100 K by measuring the magnetization as a function of temperature at 0.4 K/min (i) cooling the sample in zero dc field to 2 K, then (ii) measuring from 2 to 100 K in a dc field of 50 Oe, and finally (iii) measuring from 100 to 2 K in the same applied dc field of 50 Oe. The magnetic data were corrected for the sample holder and the intrinsic diamagnetic contributions. The SiO_2/HIPE-based precursor was measured and, as expected, was found to be diamagnetic ($–0.65\ 10^{-6}$ cm^3/g or $–39\ 10^{-6}$ cm^3/mol) with negligible paramagnetic impurities (less than 0.5 % of an $S = 1/2$ spin). The linearity of the magnetization in field at 100 K indicates also the absence of significant ferromagnetic impurities.

2.26. Mercury porosimetry. Intrusion/extrusion mercury measurements were performed using a Micromeritics Autopore IV apparatus to determine the scaffolds' macrocellular cell characteristics.

2.27. Thermogravimetric Analysis (TGA).

TGA were performed in air using a TGA 5500 Discovery TA apparatus. The heating rate was set to 5°C min^{-1} with a first temperature rump from 25°C to 180°C. We then imposed a temperature plateau of 6 hours at 180°C followed with a temperature rump from 180°C to 700°C, final temperature is maintained 6 hours. The decreasing temperature is uncontrolled and governed by the oven inertia.

2.28. Temperature programmed reduction experiments (TPR).

TPR experiments were performed on the MUB-100 materials in order to obtain information about the reducibility of their oxides phases. Prior to the TPR, the catalysts were first pretreated in situ under inert flow (Ar) for 1 h at 200 °C and cooled down to 30°C. The TPR experiments were performed with a 10 vol.% H_2/Ar gas mixture (30 mL.min^{-1}). The temperature range was 30-500°C with a ramp of 10 °C.min^{-1} and the temperature was then maintained at 500°C for 1 h. The measurements of the H_2 consumption were made in an AutoChem II/Micromeritics apparatus, using a thermal conductivity detector.

2.29. Elemental analyses.

Elemental analyses have been performed through ICP while using both ICP AES iCAP 6500 DUO and ICP AES iCAP 7400 Radia apparatus.

2.3. Quantitative porosity investigation.

2.31. Gas physisorption experiments. A Micromeritics 3Flex surface characterization analyzer (Micromeritics Instrument Corp, Norcross, GA) was used for all measurements. Prior to measurement, the samples were activated under secondary vacuum at 110°C for 12 hours. Activation at 350°C for 12 hours was also performed for comparison and led to similar results, indicating that the outgassing procedure was efficient for both temperatures. Nitrogen (N_2) adsorption isotherms measured at 77 K and argon (Ar) adsorption isotherms measured at 87 K were collected and interpreted using multi-point Brunauer-Emmett-Teller (BET) analysis for surface area determination[32] over the range 0.05–0.30 relative pressure (P/P_0) and

with a N_2 and Ar cross-sectional area of 0.162 and 0.143 nm^2, respectively. The mesoporous surface area has been determined using the Barrett, Joyner and Halenda (BJH) method while the microporous surface area has been estimated by difference between the BJH mesoporous surface area and the BET surface area, assuming that the macroporous surface area is negligible.

2.32 Helium pycnometry. Materials skeleton densities have been determined through helium pycnometry using a Micromeritics AccuPy 1330 apparatus. The samples were degassed under vacuum at 130°C for 12 hours prior performing the measurement.

2.4 Catalytic experiments. The study of the catalytic activity in the CO oxidation was performed by using a fixed bed tubular reactor containing 50 mg of the crushed sample. The reactor was continuously fed with a gas flow constituted by 11.6 mL/min of CO and 29.0 mL/min of O_2, balanced with N_2 (total flow rate = 100 mL/min), corresponding to a CO/O_2 ratio equal to 0.4 and a weight hourly space velocity (WHSV) of 120,000 $L.h^{-1}.kg^{-1}$. The reactor was put in a tubular furnace with a temperature controller, allowing the reaction temperature to be gradually increased (temperature ramp: 5 °C/min), with steps of 25°C. The effluents at the reactor outlet were analyzed on line under steady-state conditions in a Varian gas chromatograph (GC-3800) equipped with a thermal conductivity detector (TCD) (the temperatures applied for the injector, oven and detector were 150°C, 50°C and 120°C, respectively). Before the catalytic test, the sample was activated during 2 hours under an O_2-N_2 mixture (respective flow rate of 29.0 and 59.4 mL/min) at 500°C (temperature ramp: 10 °C/min).

3. Results and Discussion

The whole process of obtaining the MUB-100(x) series is depicted with the scheme 1. While considering the whole process, the most time-consuming step is the drying one, where concomitant capillarity forces have to be circumvented as far as it can be. That is the reason

why a slow drying process in a desiccator is first operated. Avoiding this step induces uncontrolled shrinkage of the gel when drying and the final monolithic character is lost. Aside, we have to note that the sol-gel process is occurring under acidic conditions (pH adjusted at 0.05, below the silica isoelectric point pH=2.1) where the silica precursors are positively charged. This feature is indeed important to explain the cobalt nano-oxides structure revealed through XRD investigations and discussed later.

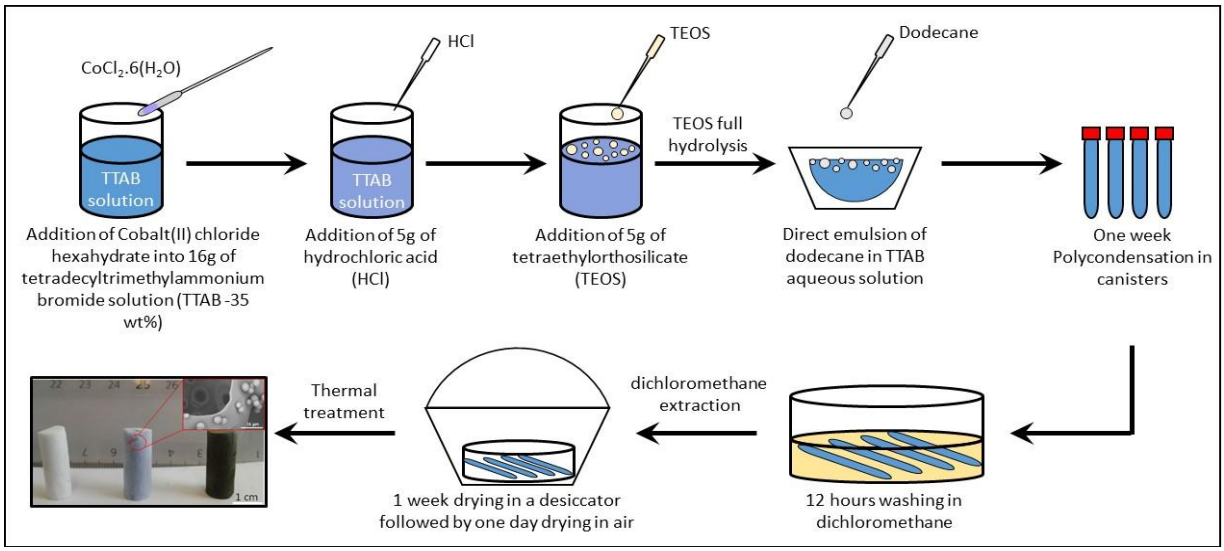

Scheme 1. Whole synthetic steps occuring for the MUB-100(x) series generation.

3.1 Materials characterization at the macroscopic length scale

When considering the Figure 1a and 1b, we can notice that the MUB-100 series are self-standing monoliths whatever the amount of cobalt introduced during the syntheses, as it is the case with traditional cobalt-free Si(HIPE) final materials.[5] When increasing the cobalt content (Table 1), the color of final materials is varying from pale blue to dark brownish, being the sign of Co_3O_4 presence in this last case, as we will see later when characterizing the materials at the microscopic length scale.

Table 1. Elemental analysis data and TGA addressing material Molar Weight (MW) and stoichiometry. *The H_2O wt% have been found by TGA under air under a heating rate of 5°C/min. The TGA can be found within the supplemental section (Fig. S1). Elemental analyses have been performed using ICP for Cobalt and Silicon atoms wt% determinations.

Sample	Co wt% Found	Co wt% Cal	Si wt% Found	Si wt% Cal	H_2O wt% Found*	H_2O wt% Cal	MW g mol^{-1}	Proposed stoichiometry
MUB-100(1)	0.62	0.62	37.2	36.7	11.2	11.1	76.50	$(Co(OH)_2)_{0.008}(SiO_{1.6}(OH)_{0.8})_{1.0}\bullet 0.47H_2O$
MUB-100(2)	1.41	1.46	37.5	36.7	10.0	9.9	76.62	$(Co(OH)_2)_{0.019}(SiO_{1.6}(OH)_{0.8})_{1.0}\bullet 0.42H_2O$
MUB-100(3)	3.23	3.10	34.3	35.0	10.9	11.2	80.18	$(Co(OH)_2)_{0.038}(Co_3O_4)_{0.0012}(Co_2SiO_4)_{0.0003}(SiO_{1.6}(OH)_{0.8})_1\bullet 0.5H_2O$
MUB-100(4)	10.1	9.9	31.6	31.0	12.0	11.7	90.93	$(Co(OH)_2)_{0.038}(Co_3O_4)_{0.035}(Co_2SiO_4)_{0.005}(SiO_{1.6}(OH)_{0.8})_1\bullet 0.59H_2O$

When performing SEM observations, typical aggregated hollow spheres (polydisperse in sizes)[5] are depicting the foams' macroporosity (Fig. 1c-h), where internal cellular junctions can be observed (Fig. 1d,f,h) addressing thus an open porosity. This macroporosity arises from the dodecane oily phase removal through the CH_2Cl_2 washing process. Aside the macroscopic cells observation, EDS investigations have been performed to assess the cobalt dispersion within the foams at the macroscopic scale (Fig. 1k-n). The general information is that whatever the cobalt concentration (Table1), the cobalt is homogeneously dispersed at the macroscale. As expected, the cobalt densities over EDS spectra being more pronounced when the cobalt concentration increases from the MUB-100(1) to the MUB-100(4). As such, we can see high density of tiny crystals over-imposed at the macroscopic wall surface for the MUB-100(4) (Fig. 1j), which are not visible when considering the MUB-100(1), MUB-100(2) and MUB-(3) materials (Fig. 1d, f, h).

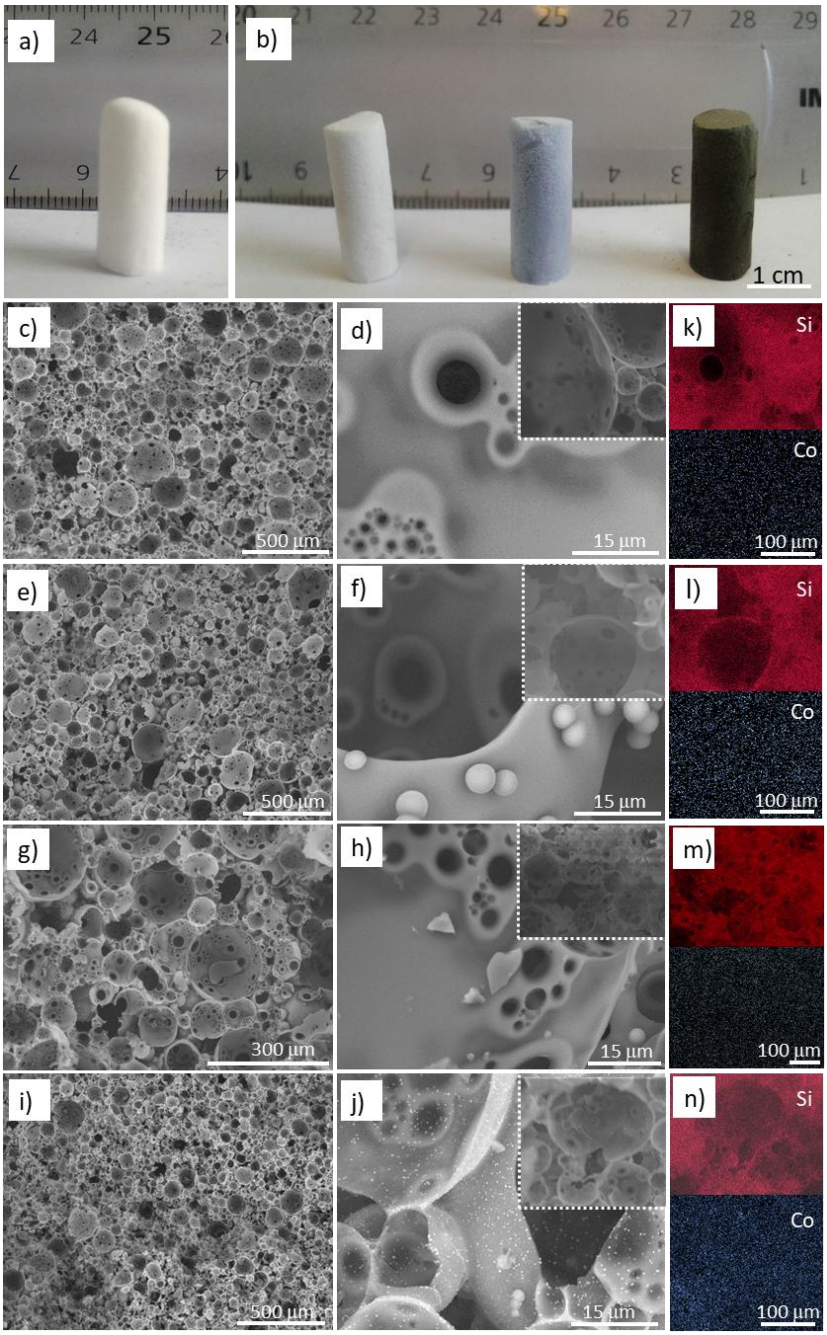

Figure 1. MUB-100 materials observation at the macroscopic length scale. a) Traditional silica based HIPE (Si(HIPE), b) from left to right MUB-100(1), MUB-100(2), and MUB-(4) where the cobalt amount is increasing. c-j) SEM images, c,d) MUB-100(1), e,f) MUB-100(2), g,h) MUB-100(3), i,j) MUB(4). k-n) EDS images, k) MUB-100(1), l) MUB-100(2), m) MUB-100(3), n) MUB-100(4). The spent areas for EDS are the ones over-imposed at the top right corners of figures d),f),h) and j).

Beyond these qualitative information, the porosity of the MUB-100 series has been evaluated by combining Mercury Intrusion Porosimetry (MIP) allowing for the determination of the bulk density (Figure 2), and helium (He) pycnometry, allowing for the determination of

the skeleton one (Table 2). The percentage of porosity has then been determined using the relation (1):

$$\% \text{ of Porosity} = [1 - (\text{bulk density}/\text{skeleton density})] * 100 \qquad (1)$$

with Porosity in % and the bulk and skeleton densities in $g.cm^{-3}$ (See Table 2).

When considering the Figure 2, we have first to emphasize that the pore size distributions are the ones corresponding to the windows that restrict the mercury infiltration. Therefore, the connecting cell-junctions, that can be seen in the Figure 1 (d,f,h,j) play a key role in this experiment, in contrast with the macroscopic cell themselves. As it is the case for Si(HIPE) materials,[5,15,16] the cell junctions are rather polydisperse from 15 to 0.1 μm with a tendency of expressing a bimodal character, being clearer for the MUB-100(4). Beyond the cell junction sizes, mercury porosimetry, in combination with He pycnometry, allows for the determination of the porosities and bulk densities (Table 2).

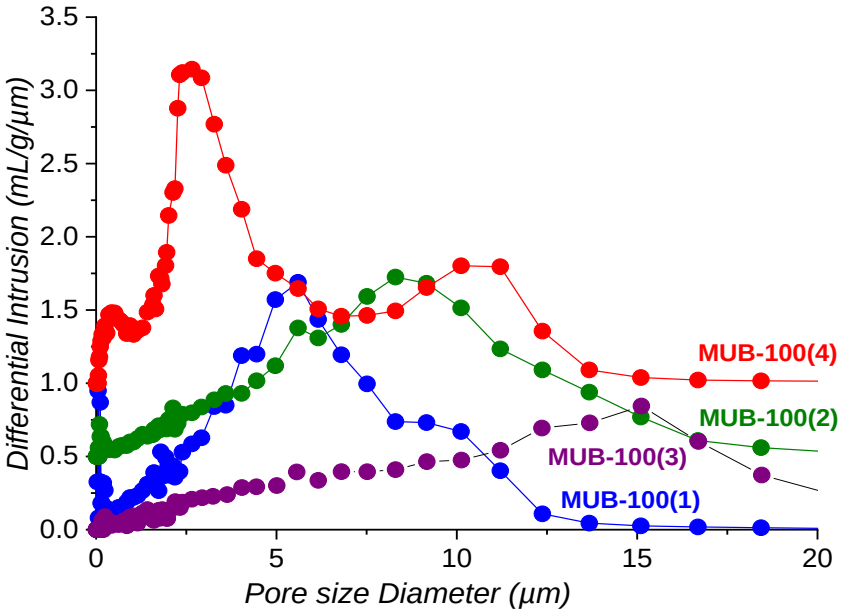

Figure 2. Pore sizes distribution obtained through mercury porosimetry. MUB-100(1) blue dots, MUB-100(2) green dots, MUB-100(3) purple dots and MUB-100(4) red dots. For the sake of clarity the MUB-100(2) and the MUB-100(4) curves have been moved upward respectively of 0.5 and 1.0 mL/g/μm.

As shown in Table 2, we can see that MUB-100(x) materials synthesized are highly porous, with a porosity around 96% for all samples. When increasing the amount of cobalt, we can observe a slight increase in the skeleton density with a disruption for the MUB-100(3) compound, while the bulk density remains constant in the limits of the error bars. The singularity of the MUB-100(3) material is discussed further with the Ar and N_2 physisorption measurements.

Table 2. Bulk density measured by Mercury Intrusion Porosimetry, skeleton density measured by Helium pycnometry and calculated porosity using equation (1).

Sample	Porosity (%)	Skeleton density (g. cm^{-3})	Bulk density (g. cm^{-3})
Si(HIPE)	96± 2%	2.22± 0.01	0.085± 0.005
MUB-100(1)	96± 2%	2.42± 0.01	0.089± 0.005
MUB-100(2)	96± 2%	2.56± 0.01	0.087± 0.005
MUB-100(3)	97± 2%	2.53± 0.01	0.083± 0.005
MUB-100(4)	97± 2%	2.60± 0.01	0.083± 0.005

3.2 Materials characterization at the mesoscopic length scale

To get further insights into the nature of the porosity of the MUB-100(x) series, argon adsorption at 87K and nitrogen adsorption at 77K have been performed for the determination of their surface area (Figure 3). All the isotherms shows adsorption at low relative pressure highlighting the presence of microporosity, and a hysteresis loop at higher relative pressure (gas capillarity condensation), more or less pronounced depending on the sample, announcing the presence of mesoporosity. We can note a slight increase of the volume adsorbed in all the adsorption isotherms at high relative pressure that is announcing the material's macroporosity. As shown in Table 3, we can see that BET surface areas are systematically lower when using Ar over N_2.

Table 3. Surface areas determined using both N_2 and Ar.

Sample	N_2-BET ($m^2.g^{-1}$)	Ar-BET ($m^2.g^{-1}$)	Smicro (N_2) ($m^2.g^{-1}$)	Smeso (N_2) ($m^2.g^{-1}$)	Smicro (Ar) ($m^2.g^{-1}$)	Smeso (Ar) ($m^2.g^{-1}$)
Si(HIPE)	930	874	425	505	271	603
MUB-100(1)	450	413	180	270	113	300
MUB-100(2)	584	530	195	389	57	473
MUB-100(3)	988	912	383	605	152	912
MUB-100(4)	439	387	133	306	31	356

This can be explained by the quadrupolar nature of the N_2 molecule, which is responsible for the specific interaction with surface functional groups and therefore the cause of the observed virtual increase in surface area. This effect is even more visible when looking at the microporous surface area (Table 3). Indeed, it is well known that, besides affecting the orientation of the N_2 molecules, these specific interactions strongly affect the micropore filling pressure, so that the pore filling pressure is not clearly correlated with the pore size. In contrast to N_2, Ar does not exhibit specific interactions with surface functional groups, thus allowing for a much more accurate surface area determination for samples presenting functional surface groups. Thus, for these reasons and based on the recommendations reported in the IUPAC technical report of 2015 on the physisorption of gases, the results obtained with Ar will be also discussed in this work. We can notice that both micro- and mesoscopic surface areas obtained through Ar physisorption measurements are drastically decreasing from the Si(HIPE) to the MUB-100 series with the exception of the MUB-100(3) material where the surface areas appear slightly higher that the Si-(HIPE) and almost double when compared with their MUB-100(x) homologues.

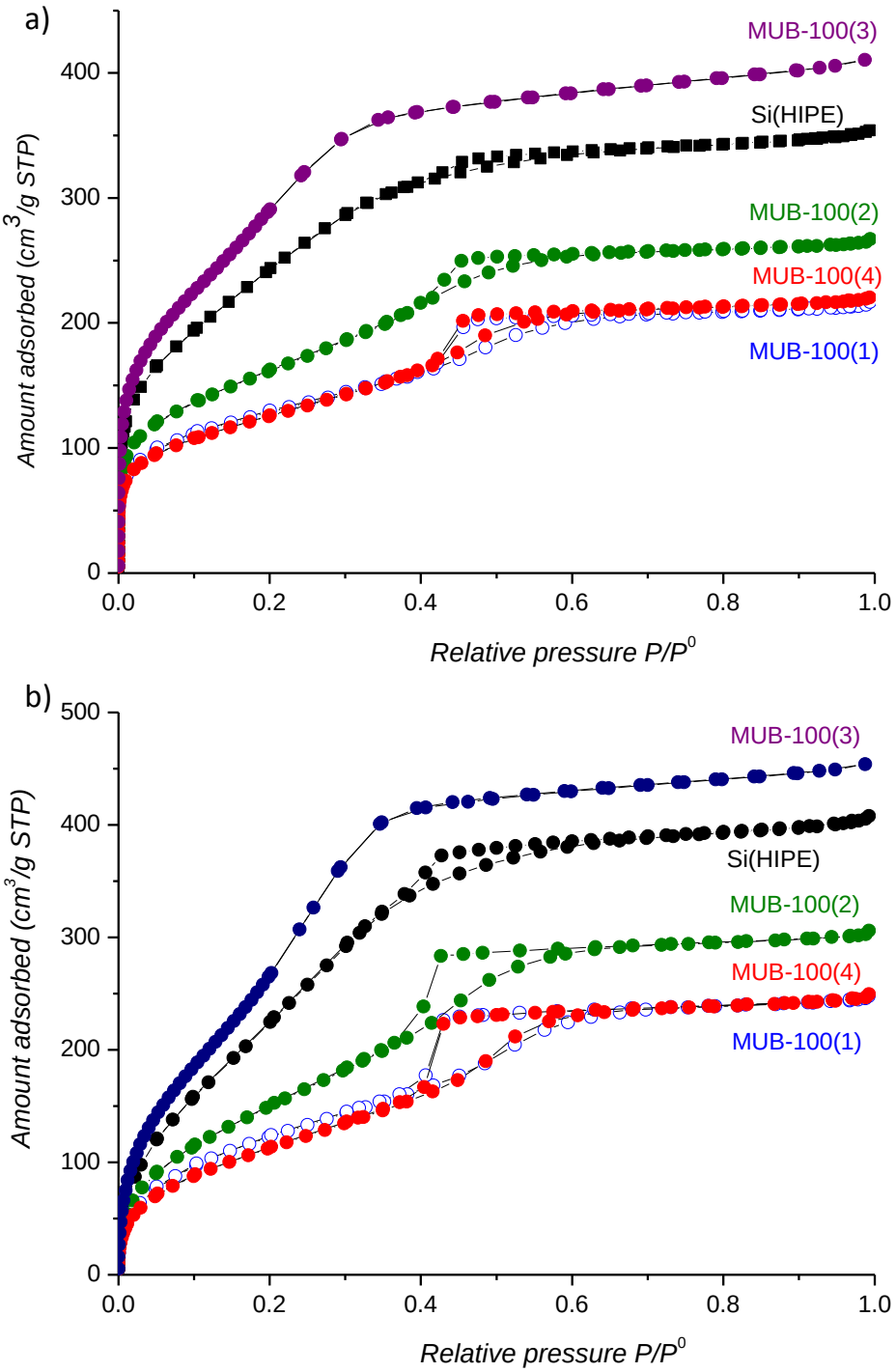

Figure 3. Gas physisorption measurements: a) N_2 adsorption-desorption curves, b) Ar adsorption-desorption curves. MUB-100(1) blue circles, MUB-100(2) green dots, MUB-100(3) purple dots and MUB-100(4) red dots.

At first glance, we can say that the decrease of surface area is totally expected as we introduce either β-$Co(OH)_2$, Co_3O_4 and Co_2SiO_4 being intrinsically denser than SiO_2. As the silica wt% is decreasing, all the micro- and mesoporosity associated with silica are decreasing

too, being less representatives of the whole materials porosity. This explanation is valid only if the silica intrinsic porosity remains constant while varying the cobalt content. Going into the details, we can notice that the microporosity from the Si(HIPE) to the MUB-100(1) is decreasing respectively from 271 $m^2.g^{-1}$ to 113 $m^2\ g^{-1}$ (Table 3) while the latter is bearing only 0.62 wt% of cobalt that is to say 8.4 10^{-5} cobalt atoms per SiO_4 tetrahedron when considering its stoichiometry (Table 1). One may argue that this decrease of microporosity is due to the increase of the skeleton density combined with some cobalt "oxo" and/or "hydroxo" clusters trapped within the inter-SiO_4 tetrahedrons microporosity, minimizing thereby its accessibility. Additionally, it has been demonstrated that the addition of Sr^{2+} or Ba^{2+} during the sol-gel-induced epitaxial growth of SiO_2 onto oriented silicon wafer favors "devitrification" that is to say, both higher packing density and organization of the SiO_4 tetrahedrons within the geometrical space, leading to α-quartz nucleation and growth instead of amorphous silica.[33] We may not exclude this "partial" process here where Co^{2+} may enhance the overall SiO_4 packing density during the polycondensation, without going here to the full "devitrification" scenario upon calcination treatment. This highest SiO_4 packing density may also intrinsically limit the MUB-100 microporosity, being lower in the case of the MUB-100(3). Still focusing on the Ar physisorption data, we can see that the MUB-100(2) material is bearing an higher mesoscopic surface area, over the MUB-100(1), despite bearing more β-$Co(OH)_2$. The tendency is the same when comparing the MUB-100(2) and MUB-100(3) materials where mesoscopic surface areas are increasing while increasing the cobalt content. This behavior is involving a "salting out" effect of the cobalt salt over the lyotrope mesophases, as discussed later in the text. Of course, this effect is also present for the MUB-100(4) but in that case the increase of the mesoscopic voids does not compensate anymore the increase of cobalt oxide content where the Co wt% is going from 1.46 to 9.90 (Table 1) resulting to a lower mesoscopic specific surface area expressed per gram of sample. Considering the mesoscopic surface areas, the MUB-

100(3) materials seems to provide the optimum configuration where both higher siliceous mesoscopic surface area is generated through a salting out effect with additional surface area emerging from higher amount of cobalt oxide nanoparticles (Fig. 4 e,f).

When addressing further the characterization at the mesoscopic length scale, we performed TEM local investigations (Figure 4). We can notice that for both MUB-100(1) (Fig. 4a, b), MUB-100(2) (Fig. 4b,c) and MUB-100(3) (Fig. 4e,f) some aggregates appear without a specific shape over mesoporous walls bearing locally a vermicular character. We intended to perform Transmission Electron Diffraction (TED) over these aggregates, which unfortunately do not diffract while considering solely the MUB-100(1) and MUB-100(2).

Considering the silica structure, poorly organized vermicular mesoscopic voids, characteristic of traditional Si(HIPE)[5] is observed. With MUB-100(4), the configuration seen through TEM is rather different. First, we can notice very distinct and well-shaped nanocrystals being polydisperse in size (10-300 nm) (Fig. 4h, i). The second main difference relies on the mesoscopic voids distribution that, in addition to the vermicular mesophase, is rather more organized and present at the vicinity of the nanocrystals (Fig. 4h, i) where hexagonal-2D organization can be locally observed. At that stage, we have to address the driving force of the co-existence of this local hexagonal 2D voids organization. Without cobalt and at the same TTAB, TEOS concentrations and pH, the hexagonal 2D phase obtained here is solely vermicular like with traditional Si(HIPE) materials.[5] Two parameters may be claimed to address this difference. First, the solvent in use in this study to wash the pre-calcined materials is not THF anymore[5] but CH_2Cl_2. The latter being poorly miscible with water will not lixiviate the tension-active molecules favoring thereby the 2D-hexagonal organization characteristic of high TTAB concentrations.

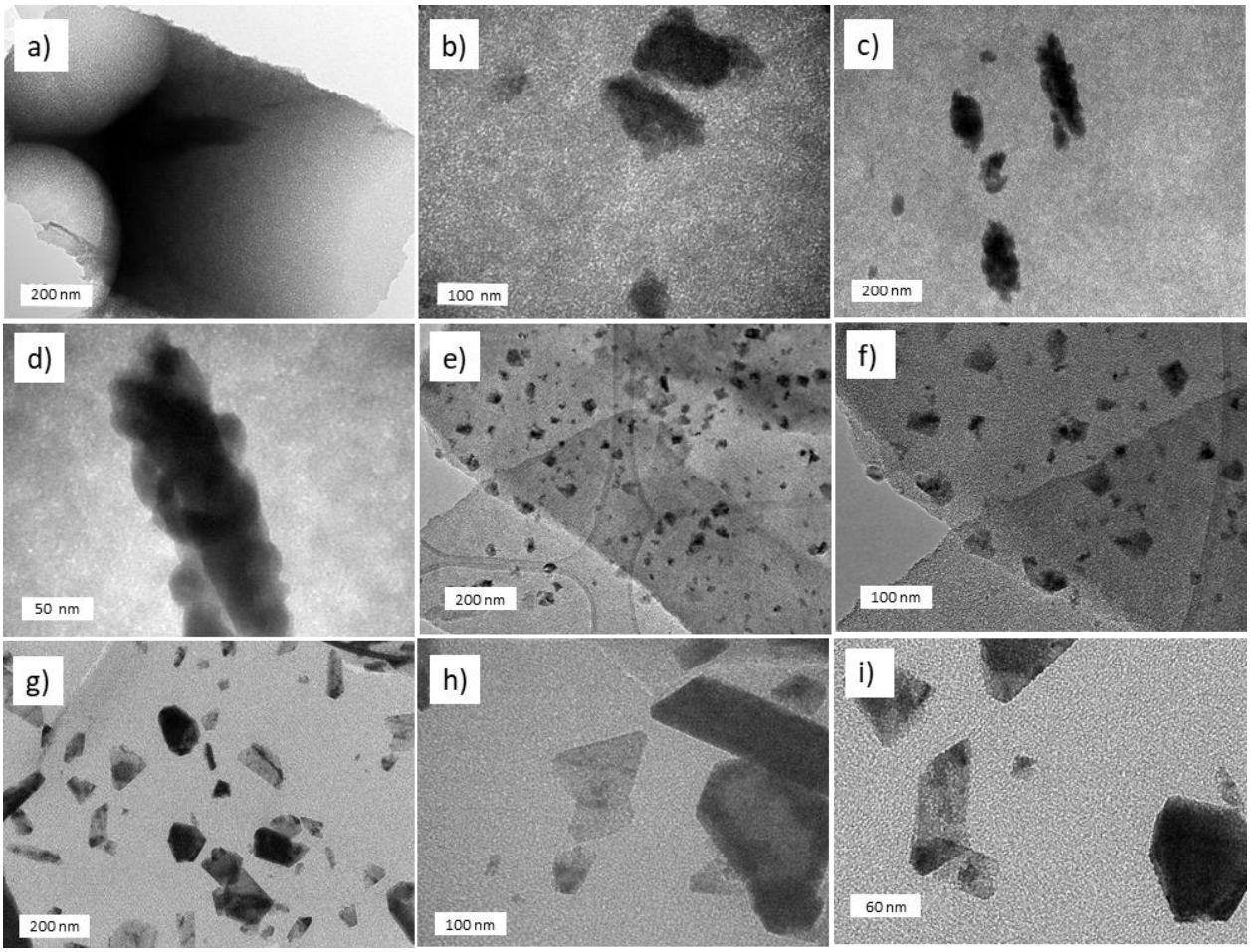

Figure 4. Investigation at the mesoscopic length scale through TEM. a,b) MUB-100(1) c,d) MUB-100(2) e,f) MUB-100(3) g-i) MUB-100(4).

The second explanation may rely on cobalt chloride salt that is providing a salting out effect[34] toward the lyotropic mesophase, minimizing the surfactant capabilities to be soluble in water. As salt concentration increases, the salting out effect will induce, through aggregation of surfactant, a higher compact configuration while reaching organized hexagonal-2D configuration of the lyotropic mesophases. This observation is in good agreement with the results reported by Dag *et al.*[35] and our previous results[15,16] when dealing on the properties of mesoporous silica particles, or SBA15-Si(HIPE) prepared either from the assembly of CTAB and P123 or only P123. In this latter report, the authors have shown that the mesopore ordering is enhanced while increasing the salt concentration. Here, we would like to mention that whatever the salt concentration, the Debye length, that quantifies the range of electrostatic

repulsion, is always of the order of 0.3 nm due to presence of oxonium (H_3O^+) electrolytes (pH is adjusted at about 0.05 with HCl, below the silica isoelectric point being around pH 2.1),[36] avoiding thus a possible electrostatic screening scenario involved towards the MUB-100 mesoporosity ordering. A third explanation of this hexagonal-2D organization present at the vicinity of the cobalt oxide crystals (Fig. 4g, h) would be a pseudo-epitaxial effect where the crystallization of the Co_3O_4 crystals during the thermal treatment will promote higher organization of the silica network at their vicinity. However, this explanation may be disregarded after establishing that the hexagonal-2D organization of the mesoscopic structure exists prior to the thermal treatment as evidenced from SAXS of the pre-calcined materials (Figure S2). Coming back to calcined materials, SAXS further supports the structural description at mesoscopic scales reached by TEM. As shown in Figure 5a, the smaller wave-vector part of the scattering intensity data exhibits, at the notable exception of the MUB-100(4) sample, the expected power-law decay with exponent -4 (Porod's law)[37] characteristic of clear-cut interfaces—here separating an "outer" empty medium (air) from an "inner" filled medium (silica). The significant departure from Porod's law observed for the MUB-100(4) sample with a decay following a power-law with exponent -3, associated to a broad feature at small angles (*ca.* 0.06 $Å^{-1}$), is attributed to the presence of cobalt-rich nanocrystals segregated from the silica matrix, as suggested by the TEM data (Fig. 4g,h). The diffraction peak associated to the hexagonal-2D organization of the mesoscopic structure (Figs. 5a, 5b) is always found at larger angles in the calcined materials, as especially clear in the Porod representation used in Figure 5b. The calcination also obviously increases disorder (compare to Fig. S2, with the so-called "second order" peak less pronounced or absent) in addition to making the structure more compact. Another important point to address is the fact that for the MUB-100(4) and despite a synthetic Si/Co molar ratio of 0.57 the Co_3O_4 crystal sizes remain at the nanoscopic length scale, reaching 200-300 nm at most (Fig. 4g).

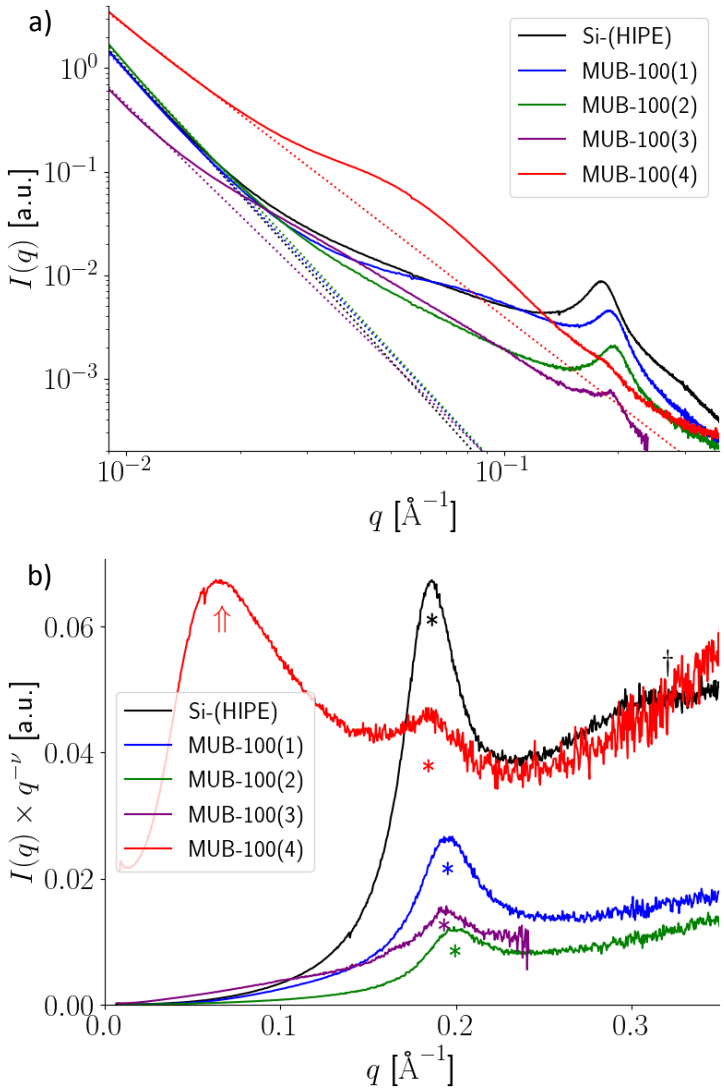

Figure 5. a) Small-angle scattering intensities (double logarithmic scale) for the reference Si-(HIPE) sample (black), and the three MUB-100(1) (blue), MUB-100(2) (green), MUB-100(3) (purple) and MUB-100(4) (red) samples. The colored dotted lines correspond to power-law decaying intensities with exponents close to -4 (Porod's law) except for the MUB-100(4) sample where the exponent is found close to -3. b) Porod-like representation of the small-angle intensities scattered by the calcined materials, emphasizing the mesoporous structure of the reference Si-(HIPE) sample (black), and of the three MUB-100(1) (blue), MUB-100(2) (green), MUB-100(3) (purple) and MUB-100(4) (red) samples (ν is close to -4 as expected from Porod's law, except for the MUB-100(4) sample where its value is found close to -3). The colored star marks the q^* location in reciprocal space of the characteristic structural peak arising from the 2D hexagonal phase used for the synthesis. Note that for the reference Si-(HIPE) sample a "second order" peak may be found at roughly $\sqrt{3}$ the "first order" peak (dagger symbol)—as expected for hexagonal 2D order. Associated structural parameters (derived from $2\pi/q^*$): Si-(HIPE) 3.38 nm, MUB-100(1) 3.21 nm, MUB-100(2) 3.14 nm, MUB-100(3) 3.24 nm and MUB-100(4) 3.40 nm. Note the presence at about $2\pi/100$ Å^{-1} (upwards double arrow symbol), and for MUB-100(4) only, of a broad feature possibly associated to Co_3O_4 nanocrystals.

This trend is certainly due to the synthetic sol-gel acidic condition where the silica network will bear a strong fractal character[36] rather than Euclidean. As such, the silica net-

work fractal character will show high specific surface where the Co_3O_4 nucleation enthalpy will be minimized, favoring the nucleation events towards the crystals growth, minimizing thereby their sizes. This feature is of importance when dealing with heterogeneous catalysis, as we will see later.

3.3 Materials characterization at the microscopic length scale

At the microscopic length scale, we first performed X-ray diffraction (XRD) to address the cobalt oxide phases present within the MUB-100 series (Figure 6).

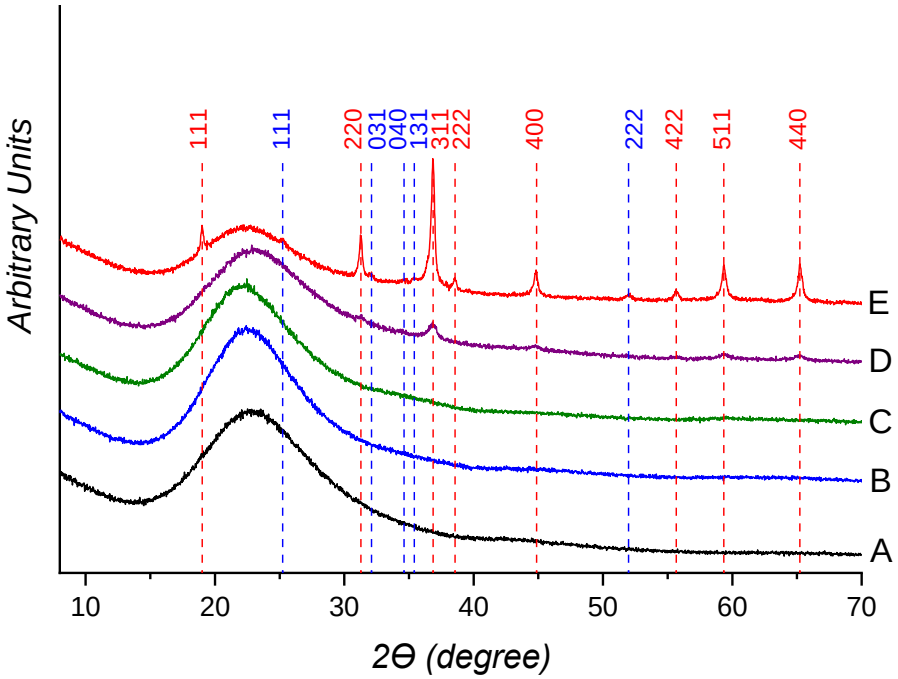

Figure 6. XRD investigations: A) Si(HIPE) sample (black), B) MUB-100(1) (blue), C) MUB-100(2) (green), D) MUB-100(3) (purple) and E) MUB-100(4) (red). Red dash (111), (220), (311), (222), (400), (422), (511) and (440) main Bragg diffraction peaks of the Co_3O_4 cubic phase (JCPDS card No. 74-1657). Blue dash (111), (031), (040), (131) and (222) main diffraction peaks that correspond to the Co_2SiO_4 olivine phase (JCPDS card No. 84-1298).

We can notice that for the MUB-100(1) and MUB-100(2) materials there is no Bragg peaks, in agreement with the TED investigations. We can observe only a broad hump centered at 23-24° (2Θ) that corresponds to the amorphous silica network (statistical repartition of the SiO_4 tetrahedron).[5] Considering the MUB-100(3), XRD assesses the presence of spinel Co_3O_4

(Fig. 6D). We have performed aside TEM-TED (Figure S3) that shows additionally the presence Co_2SiO_4 nanostructures. For the MUB-100(4), XRD investigations evidence the presence of a biphasic system made of Co_3O_4 and Co_2SiO_4 (Fig. 6E), meaning that the phase Co_2SiO_4 is growing while increasing the Cobalt content. Unfortunately, both XRD and TEM/TED investigations were unsuccessful (no Bragg peaks detected) for the MUB-100(2) and MUB-100(1) materials. Considering the pale blue color of the MUB-100(1) monolith (Fig. 1b), we first intuited that the phase present was amorphous Co_2SiO_4,[38] but this phase is normally appearing only above 1100°C when addressing acidic based-syntheses,[38] while the thermal treatment applied here is reaching a maximum temperature of 700°C. To get the spinel Co_2SiO_4 at relatively low temperature the synthetic path should be addressed under alkaline conditions (above the silica isoelectric point) where the Co^{2+} species will have molecular affinity with the negatively charge silicate precursors.[39] In the present cases, the Co_2SiO_4 phase appears only above 3wt% of Co (Table 1, Fig. 6), certainly for the Co^{2+} species to be concentrated highly enough to both circumvent phase separation between positively charge siliceous precursors and the Co^{2+} and optimize the Co thermal diffusion when the thermal treatment is applied. On the contrary, at low Cobalt wt%, the phase separation between siliceous precursor and silica is effective during the sol-gel synthetic step, while providing the β-$Co(OH)_2$ embedded within the siliceous host when the thermal treatment is applied. As the β-$Co(OH)_2$ phase is amorphous, we have decided to run magnetic susceptibility (χ) experiments in order to collect more information on the chemical structure of the MUB-100(1) and MUB-100(2), that present a lower cobalt content. As such, magnetic properties of the MUB-100(1) and MUB-100(2) materials have been studied using dc susceptibility measurements. In agreement with a paramagnetic behavior, the temperature dependence of the reciprocal susceptibility ($1/\chi$) is linear above 50 K for the two materials. They can be fitted to a Curie-Weiss law ($\chi_{CW} = C/(T-\theta)$) with Curie constants of C = 0.0287 and 0.0656 cm^3 K mol^{-1} and

Weiss temperature of θ = +7.6 and +5.6 K for MUB-100(1) and MUB-100(2), respectively (left part of Figure S4). Based on these positive Weiss constants, ferromagnetic interactions are dominant in these materials likewise the bulk β-$Co(OH)_2$ phase, which displays an antiferromagnetic order below 12.3 K.[40,41] Curie constants are consistent with the expected amount of S = 3/2 Co^{2+} centers. When normalized for one S = 3/2 Co^{2+} center, the Curie constant are 3.59 and 3.45 cm^3 K mol^{-1} for MUB-100(1) and MUB-100(2) respectively, which corresponds to large g factors of 2.77 and 2.71 expected for S = 3/2 Co^{2+} systems.[42] Above 100 K and in agreement with the $1/\chi$ *vs* T data, the χT products for MUB-100(1) and MUB-100(2) are almost constant to the above estimated Curie constants (right part of Figure S4). At lower temperatures, the χT product increases and shows a clear maximum around 8.2 K confirming the presence of dominant ferromagnetic interactions. Zero-Field-Cooled (ZFC)–Field-Cooled (FC) experiments have been performed below 100 K (left part of Figure S5). A bifurcation of the ZFC/FC data is observed below 5 K indicating the presence of magnetic bistability likely associated to surface effects of β-$Co(OH)_2$ nanoparticles and the blocking of the magnetization (with a blocking temperature T_B around 3.8 K at 0.4 K/min).[40] The field dependence of the magnetization (M) at 2 K confirms the presence of a magnetic bistability (hysteresis) as shown in the right part of Figure S5. At 9 T, the magnetization is almost saturated to 0.0205 and 0.0549 μ_B for MUB-100(1) and MUB-100(2), respectively. These values correspond to 2.6 and 2.9 μ_B per Co^{2+} ions in agreement with the presence of a large Co^{2+} zero-field splitting, which induces a marked decrease of the magnetic moment. At 2 K, the remnant magnetizations are 0.0036 and 0.0083 μ_B with associated coercive fields of 870 and 710 Oe for MUB-100(1) and MUB-100(2) (at 0.2 T/min), respectively. Overall, the magnetic properties of the MUB-100(1) and MUB-100(2) materials are consistent with their respective chemical composition (Table 1) and the presence of superparamagnetic β-$Co(OH)_2$ nanoparticles as already described in the literature.[40,41] For MUB-100(4), $1/\chi$ *vs* T plot is also linear above 50

K, that can be fitted to a Curie-Weiss law with C = 0.284 cm^3 K mol^{-1} and θ = –13.8 K (left part of Figure S4). As for MUB-100(1) and MUB-100(2), this material is paramagnetic but, in this case, dominant antiferromagnetic (AF) interactions between spin carriers are detected as expected in presence of bulk Co_3O_4.[42] Based on the chemical composition (Table 1), the Curie constant per Co^{2+} is 3.42 cm^3 K mol^{-1}, which includes the Co^{2+} sites of the β-$Co(OH)_2$, Co_3O_4 and Co_2SiO_4 phases (implying an average g factor of 2.70; it is worth mentioning that Co^{3+} are diamagnetic metal ions). When decreasing the temperature, the χT product slightly decreases down to 50 K, confirming the presence of dominant AF interactions in the material (right part of Figure S4). The maximum of the χT product at 8.2 K (inset of Figure S4 right part) and the ZFC/FC data below 5 K (inset of Figure S5 left part) confirm the presence of the superparamagnetic β-$Co(OH)_2$ nanoparticles as already observed in MUB-100(1) and MUB-100(2). In the χT *vs* T data shown in Figure S4 (right part), a clear anomaly at 45 K is observed, which is likely the reminiscent of the antiferromagnetic order expected in bulk Co_3O_4.[39] In the same temperature range, the ZFC/FC data in Figure S5 (left part) show also a bifurcation point suggesting the presence of a magnetization blocking typical of superparamagnetic Co_3O_4 nanoparticles.[42] The M *vs* H data at 2 K, shown in the right part of Figure S5, exhibits a hysteresis loop with a coercive field of 500 Oe, similarly to that observed for MUB-100(1) and MUB-100(2) and in agreement with the blocking of the β-$Co(OH)_2$ nanoparticles. At 2 K, the remnant magnetization is 0.010 μ_B while the magnetization value at 9 T is 0.132 μ_B which corresponds to 1.59 μ_B per Co^{2+} ion (inset of Figure S5 right part). The magnetic properties of MUB-100(3) are similar to those measured for MUB-100(1) and MUB-100(2), indicating a predominant β-$Co(OH)_2$ phase. $1/\chi$ *vs* T plot is linear above 50 K and can be fitted to a Curie-Weiss law with C = 0.0994 cm^3 K mol^{-1} and θ = +11.4 K (left part of Figure S4). This material is thus paramagnetic with dominant ferromagnetic interactions between spin carriers. The maximum of the χT product at 8.2 K, the diver-

gence of the ZFC/FC data below 5 K (Figure S5 left part; at 0.4 K/min) and the hysteresis of *M vs H* plot (with a coercive field of 810 Oe at 0.2 T/min; Figure S5 right part) confirm the presence of the superparamagnetic β-$Co(OH)_2$ nanoparticles. No clear magnetic signature of the Co_3O_4 phase (i.e. bifurcation on the ZFC/FC data around 45 K as seen for MUB-100(4)) is observed. Nevertheless, considering only the presence of the β-$Co(OH)_2$ phase (i.e. only Co^{2+} ions), the Curie constant per Co^{2+} site is surprisingly low around 2.21 cm^3 K mol^{-1} (implying an average *g* factor of 2.17). Taking into account the presence of few percent of Co^{3+} diamagnetic metal ions and the Co^{2+} metal ions from the β-$Co(OH)_2$, Co_3O_4 and Co_2SiO_4 phases as reported in Table 1, the Curie constant per Co^{2+} reaches 2.50 cm^3 K mol^{-1} (implying an average *g* factor of 2.31) and becomes more reasonable based on previously reported systems. At 2 K, the remnant magnetization is 0.014 μ_B while the magnetization value at 9 T is 0.072 μ_B corresponding to 1.81 μ_B per Co^{2+} ion. It is worth noting that the presence of the Co_2SiO_4 phase is not confirmed by the magnetic measurements on these four samples. For MUB-100(3) and MUB-100(4), this apparent discrepancy is indeed well explained by the extremely small quantity of the Co_2SiO_4 phase detected by other physical characterizations (Table 1). To summarize, the chemical compositions given in Table 1 with the presence of the different magnetic phases, β-$Co(OH)_2$, Co_3O_4 and Co_2SiO_4, are qualitatively and quantitatively coherent with the reported magnetic measurements.

3.4 CO oxidation through heterogeneous catalysis

The catalytic performances of the MUB-100 series were evaluated in the oxidation of carbon monoxide with oxygen. CO is a colorless, odorless, tasteless, and non-irritating gas, which makes it very difficult for humans to detect, but it is a poisonous gas to all life forms that respire due to its high affinity with hemoglobin. The catalytic oxidation of CO is a very important reaction in many applications such as in automotive and residential air cleaning

technologies, gas masks for firefighters, CO detectors, and selective oxidation of CO in reformer gas for fuel cell applications.[44,45] Commercial catalysts for CO oxidation are mainly constituted of noble metals, which remain too expensive to be further used widely. Therefore, more attention has been paid for developing efficient and low-cost oxidation catalysts.

The CO oxidation reaction towards CO_2 is based on a competitive mechanism of adsorption on the active sites between the CO and O_2 molecules.[46] In this study, the CO/O_2 ratio used was equal to 0.4, corresponding to a value allowing to work in appropriate experimental conditions. Indeed, for this reaction, the O_2 adsorption at the surface of the catalysts is known to be much weaker than the CO one. Consequently, even with a low CO/O_2 ratio, the active sites are not blocked by the presence of higher quantity of O_2 molecules.[47] In addition, an excessive CO concentration in the fed gaseous mixture may cause a decrease in the catalytic activity by hindering the adsorption and dissociation of active O_2 molecules. Figure 7 displays the catalytic performances of the four MUB-100 materials during the CO oxidation as a function of the reaction temperature. The results are presented in terms of CO conversion (Fig. 7 left part) or specific activity (Fig. 7 right part) representing the quantity of CO mol converted to CO_2 per second divided by the mass of Co (active species) contained in the evaluated sample ($mmol_{(CO)}.g_{(Co)}^{-1}.s^{-1}$).

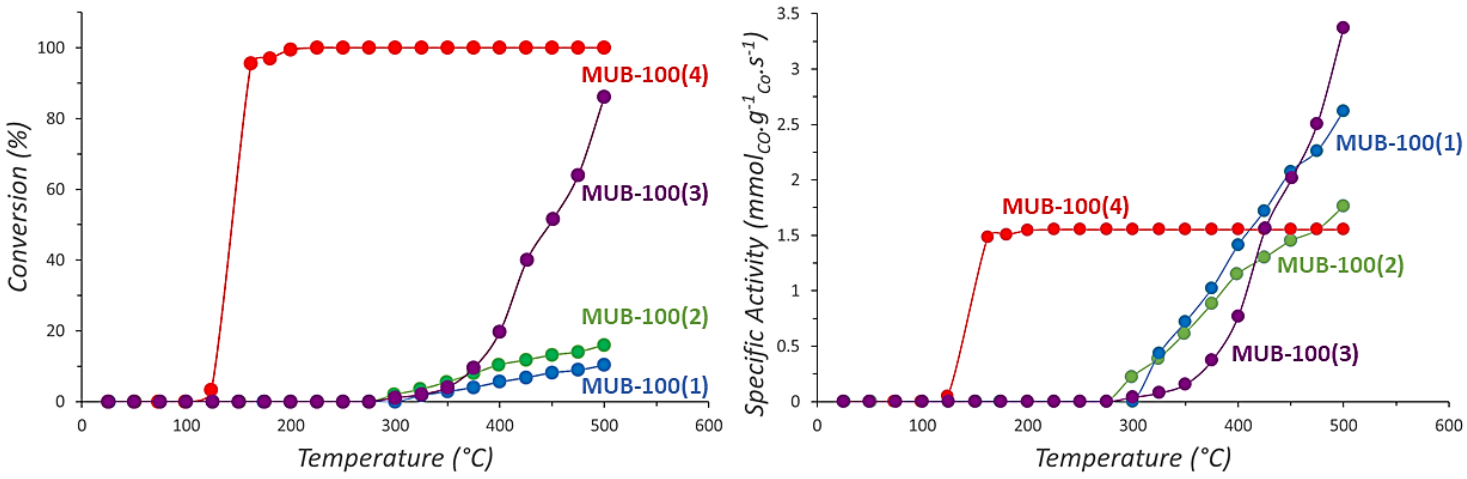

Figure 7. Left: CO conversion (%) *vs* temperature for MUB-100(1) (blue dots), MUB-100(2) (green dots), MUB-100(3) (purple dots) and MUB-100(4) (red dots). Right: Specific activity *vs* temperature

for MUB-100(1) (blue dots), MUB-100(2) (green dots), MUB-100(3) (purple dots) and MUB-100(4) (red dots).

Among the four catalysts, only the MUB-100(4) was able to totally convert the CO before 500°C under the experimental conditions used, achieving 50% of conversion for a light-off temperature T_{50} of 145°C. This T_{50} value reveals a high efficiency for the MUB-100(4) in CO oxidation, since catalysts presenting similar composition (10 wt%Co/SiO_2) were found much less active in the literature. For instance, Lima *et al.* prepared two Co/SiO_2 catalysts (with 10 wt%) by sol-gel one pot (Op) and impregnation (Im) methods, and obtained T_{50} values around 425°C (Op sample) and 270°C (Im sample) under operating conditions similar to the ones used here.[48] With a 12 wt%Co/SBA-15 catalyst prepared by impregnation of cobalt acetate on sol-gel SBA-15 material, Kuboňová *et al.*[49] observed a T_{50} temperature of 164°C under experimental conditions more propitious since they used a feed containing 0.1 mol%CO with WHSV = 60,000 $L.h^{-1}.kg^{-1}$ compared in this study to 11.6 mol%CO with WHSV = 120,000 $L.h^{-1}.kg^{-1}$. Several authors have reported that generally Co-silica materials give poor performances in CO oxidation in contrast to Co-alumina or Co-titania, due to the weak interactions existing between silica and cobalt oxide leading to the sintering of Co species during the thermal treatment.[17,50] The synthetic path used in this study to design the $CoOx\text{-}SiO_2$(HIPE) macro-mesocellular (MUB-100) catalysts seems then efficient to maintain the high dispersion of the cobalt species while ensuring a high accessibility to the active sites. Indeed, the "one pot" synthetic path operating at low pH will promote a silica network with a fractal character that favors cobalt oxide nucleation events versus their growth, implying the tendency of generating nanocrystals. As "one pot" syntheses, the native nanocrystals are embedded within the silica network but still accessible through the mesoscopic voids. Beyond, the presence of a noticeable quantity of Co_3O_4 nanoparticles in the MUB-100(4) sample can also contribute to explain its high conversion. This spinel structure is considered

as the most active of the three cobalt oxides CoO, Co_2O_3 and Co_3O_4.[51-53] To corroborate this point, the MUB-100(4) sample was reduced under hydrogen flow as follows: MUB-100(4) sample was placed in a cylindrical furnace and pure H_2 was introduced until reaching a pressure of 2 bar. Then the sample was vacuumed for 3 minutes. This process was repeated 3 times to ensure the lowest O_2 content in the furnace. Then, the sample was submitted to pure hydrogen flow (with a slight over pressure of 1.05 bar) and the temperature was increased to 400°C at 10°C min^{-1}. After 1 day, the sample was cooled down to room temperature still under H_2 flow. When the temperature reached 50°C, the hydrogen flow was stopped while maintaining the pressure at 1.05 bar. The reduced MUB-100(4) material being now amorphous (Figure S6) was then evaluated for CO oxidation (Figure S7) revealing a decrease of the catalytic performances for CO oxidation. The TPR profile obtained during the reduction process (reported in Figure S8) shows that the reduction of the oxidized species occurs in a temperature range comprised between 330 and 430°C, the maximum of the consumption peak being located at 384°C. This peak is generally associated to the reduction of Co_3O_4 species to CoO.[52-54] Actually, the H_2 consumption deduced from the TPR profile (489 µmol $H_2.g^{-1}$(catalyst)) appears in good agreement with the quantity necessary to reduce all the Co_3O_4 phase contained in the MUB-100(4) sample considering the stoichiometry given in Table 1 and following the reduction reaction (2):

$$Co_3O_4 + H_2 \rightarrow 3\ CoO + H_2O \qquad (2)$$

The absence of a second peak on the TPR profile for the reduction of Co^{2+} to Co° can be linked to the formation of cobalt silicate species, stabilizing the +II oxidation state due to Co species in strong interaction with the silica support, generally needing a higher temperature (> 600°C) to be reduced.[48] Consequently, it seems that the reduction of the Co_3O_4 phase is unfavorable on the catalytic performances. The catalytic experiments being performed with the same mass of catalyst (50 mg) whatever the MUB-100 sample, it is

logical that for a given temperature, the CO conversion in Fig. 7 (left) evolves accordingly with the Co content in the following order: MUB-100(4) > MUB-100(3) > MUB-100(2) > MUB-100(1). One may argue that this effect is due to lowering the materials intrinsic heat capacities while increasing the Co content. However, this is not the case when considering the Figure S9, we can notice that whatever the temperature range the material heat capacities evolve as followed: MUB-100(4) > MUB-100(3)> MUB-100(2) > MUB-100(1). Aside, the specific activity calculated from the conversion values allows comparing the performances of the four MUB-100 samples on the basis of a same Co mass. It must be emphasized that for conversion values reaching 100% (case of the MUB-100(4) material), the calculation of the specific activities per g of Co is underestimated since the mass of Co present in the sample exceeds necessarily the quantity needed to totally convert the CO molecules. The results given in Fig. 7 (right) show the MUB-100(3), MUB-100(2) and MUB-100(1) materials do not convert CO before 275-300°C (compared to 125°C in the case of MUB-100(4)). For these samples, the CO conversion remains below 20% but between 325-400°C. Finally, the specific activities of the less loaded catalyst (MUB-100(1)) are in general superior to the ones displayed by MUB-100(2) and MUB-100(3) indicating the presence of a higher quantity of active species in this sample, probably resulting from a better dispersion of the cobalt entities. Despite the presence of a Co_3O_4 phase on the MUB-100(3) material, this sample displays a specific activity higher than those of the MUB-100(1) and MUB-100(2) catalysts only after 450°C, indicating that the quantity of Co species involved in this Co_3O_4 phase remains here too limited.

Finally, the catalyst thermodynamic stabilities have been verified while cycling (Figure S10) indicating a very minimal evolution of the catalytic performances of the MUB-100(4) material during four consecutive cycles of CO oxidation (the catalyst not having undergone any heat treatment between each cycle).

4. CONCLUSIONS

Through the integrative chemistry synthetic path[56], we have combined sol-gel process and physical chemistry of complex fluids to generate the first series of mixed oxides CoOx-SiO_2(HIPE) macro-mesocellular monolithic materials, labeled MUB-100(x). These porous materials are bearing an average porosity of 94%. At the mesoscopic length scale, the voids organization is biphasic vermicular-hexagonal 2D where the hexagonal 2D is retained further after calcination at 700°C while increasing the cobalt concentration during the materials formulation. The materials depict surface areas between 400-500 m^2 g^{-1} assessed through Ar physisorption investigations. For the lowest cobalt concentrations MUB-100(1) and MUB-100(2), magnetism measurements reveal the β-$Co(OH)_2$ nature of the nanocrystals embedded within the silica matrix while the XRD patterns depict an amorphous character. Considering the mixed oxides bearing the highest cobalt content, the systems is biphasic with both the Co_3O_4 spinel and the Co_2SiO_4 olivine structures. The one pot synthetic path is operating at low pH, promoting thus a silica network with a fractal character. This type of silica network is favoring cobalt oxide nucleation events versus their growth favoring the generation of nanocrystals, which is true even at the starting silica/cobalt molar ratio of 0.57 for the MUB-100(3) compound. These porous materials have further been tested towards the CO oxidation into CO_2. Considering this catalytic application, the MUB-100(4) was able to totally convert the CO flow before 200°C (starting at 125°C) while achieving 50% of conversion for a light-off temperature T_{50} of 145°C, enlightening thereby the high efficiency of the MUB-100(4) regarding CO oxidation. On the other hand, we showed that the specific activity normalized per the Co mass depicts a cross-over where the MUB-100(3), MUB-100(2) and MUB-100(1), that do not convert CO before 275-300°C, present superior specific activities at high temperature compared to MUB-100(4). We have thus applied hydrogen-based partial reduction to the MUB-100(4) material in order to express further the Co^{2+} species abundance

and/or to create amorphous β-$Co(OH)_2$ based supported catalyst. This material appeared less active than the non-reduced analogue MUB-100(4) material indicating a lower activity for the CO oxidation of the cobalt (II)-type species compared to the Co_3O_4 phase.

ASSOCIATED CONTENT

Supporting Information is available free of charge at https://xxxxxxxxxxxxxxxxxxxxxxxxxxxxxxxxxxxxxxxxxxxxxxxxxx

TGA experiments, Porod-like representation of the small-angle scattered intensities, Transmission Electron nano-Diffraction, magnetic susceptibility versus temperature, WAXS of the reduced MUB-100(4), CO conversion (%) *vs* temperature for MUB-100(4) and Reduced MUB-100(4), TPR of the MUB-100(4) material, MUB-100 series heat capacities, MUB-100(4) effectiveness toward CO-oxidation while cycling. (PDF)

AUTHOR INFORMATION

Corresponding Authors

Rénal Backov - Université de Bordeaux, CRPP-UMR CNRS 5031, 115 Avenue Albert Schweitzer, 33600 Pessac, France. https://orcid.org/0000-0001-5946-8917 ; E-mail: renal.backov@crpp.cnrs.fr

Catherine Especel - Institut de Chimie des Milieux et Matériaux de Poitiers (IC2MP), UMR 7285 CNRS - Université de Poitiers, 4 rue Michel Brunet, TSA 51106, 86073 Poitiers Cedex 9 – France. https://orcid.org/0000-0002-4066-6515 ; E-mail: catherine.especel@univ-poitiers.fr

Authors

Isabelle Ly- Université de Bordeaux, CRPP-UMR CNRS 5031, 115 Avenue Albert Schweitzer, 33600 Pessac, France. https://orcid.org/0000-0001-5357-9106

Antoine Vardon- Université de Bordeaux, CRPP-UMR CNRS 5031, 115 Avenue Albert Schweitzer, 33600 Pessac, France. https://orcid.org/0000-0002-3182-5879

Nicolas Chanut - Massachusetts Institute of Technology, Department of Civil and Environmental Engineering, 77, Mass. Avenue, Cambridge MA 02139, USA. https://orcid.org/0000-0002-5159-9901

Frédéric Nallet - Université de Bordeaux, CRPP-UMR CNRS 5031, 115 Avenue Albert Schweitzer, 33600 Pessac, France. https://orcid.org/0000-0002-1792-0511

Roland J. Pellenq - Massachusetts Institute of Technology, Department of Civil and Environmental Engineering, 77, Mass. Avenue, Cambridge MA 02139, USA. https://orcid.org/0000-0001-5559-4190

Mathieu Rouzières - Université de Bordeaux, CRPP-UMR CNRS 5031, 115 Avenue Albert Schweitzer, 33600 Pessac, France. https://orcid.org/0000-0003-3457-3133

Rodolphe Clérac - Université de Bordeaux, CRPP-UMR CNRS 5031, 115 Avenue Albert Schweitzer, 33600 Pessac, France. https://orcid.org/0000-0001-5429-7418

Joudia Akil - Institut de Chimie des Milieux et Matériaux de Poitiers (IC2MP), UMR 7285 CNRS - Université de Poitiers, 4 rue Michel Brunet, TSA 51106, 86073 Poitiers Cedex 9 – France. https://orcid.org/0000-0002-8638-2868

Florence Epron - Institut de Chimie des Milieux et Matériaux de Poitiers (IC2MP), UMR 7285 CNRS - Université de Poitiers, 4 rue Michel Brunet, TSA 51106, 86073 Poitiers Cedex 9 – France. https://orcid.org/0000-0002-7720-1578

Author contributions

The manuscript was written through contributions of all authors.

Notes

The authors declare no competing financial interest.

Funding

The authors wish to thank the CNRS and the University of Bordeaux, the Région "Nouvelle Aquitaine" and the Quantum Matter Bordeaux.

ACKNOWLEGMENTS

RB wishes to thank Ahmed Bentaleb for acquiring all the SAXS and WAXS data sets, Dr. Marie-Anne Dourges (ISM) for the poro-mercury data acquisitions, Dr. François Dole for acquiring the heat capacities *versus* temperature, Sabrina Lacomme (Bordeaux Imaging Center- BIC) for the TEM investigations, Dr. François Weill (Placamat-ICMCB) for TEM-TED investigations. Mr Eric Lebreau is thanked (ICMCB) for the XRD-investigations. We are thankful to Professor Jean-Louis Bobet (ICMCB) for the MUB-100(4) material H_2 reduction and Ms. Emily Bloch for the MUB-100(3) N_2, Ar physisorption acquisitions (Madirel, Marseille).

References

(1) Silverstein, M. S. Recent advances in emulsion-templated porous polymers. *Prog. Polym. Sci.* **2014**, *39*, 199−234.

(2) Silverstein, M. S. Emulsion-templated polymers: Contemporary contemplations. *Polymer* **2017**, *126*, 261−282.

(3) Silverstein, M. S. The Chemistry of Porous Polymers: The Holy Grail, *Israel. J. Chem*. **2020**, *60*, 140−150.

(4) Araya, A. Hydrophobic, Highly Porous, Three-Dimensional Inorganic Structures. *US Patent 4888309*, **1989**.

(5) Carn, F.; Colin, A.; Achard, M.-F.; Deleuze, H.; Sellier, E.; Birot, M.; Backov, R. Inorganic monoliths hierarchically textured via concentrated direct emulsion and micellar templates. *J. Mater. Chem.* **2004**, *14*, 1370−1376.

(6) Brun, N.; Ungureanu, S.; Deleuze, H.; Backov, R. Hybrid foams, colloids and beyond: From design to applications, *Chem. Soc. Rev.* **2011**, *40*, 771−788.

(7) Roucher, A.; Depardieu, M.; Pekin, D.; Morvan, M.; Backov, R. Inorganic, hybridized and living macrocellular foams: "Out of the Box" heterogeneous catalysis. *Chem. Record.* **2018**, *18*, 776−787.

(8) Roucher, A.; Morvan, M.; Pekin, D.; Depardieu, M.; Blin, J.-L.; Schmitt, V.; Baret, J.-C.; Backov, R. From Compartmentalization of Bacteria within Inorganic Macrocellular Beads to the Assembly of Microbial Consortia. *Adv. Biosystems* **2018**, *2*, 201700233.

(9) Brun, N.; Babeau-Garcia, A.; Achard, M.-F. ; Sanchez, C.; Durand, F.; Guillaume, L.; Birot, M.; Deleuze, H.; Backov, R. Enzyme-Based Biohybrid Foams Designed for

Continuous Flow Heterogeneous Catalysis and Biodiesel Production. *Energy § Environmental Science* **2011**, *4*, 2840−2844.

(10) Gaikwad, P.; Ungureanu, S.; Backov, R.; Vynck, K.; Vallée, R.A.L. Photon transport in cylindrically-shaped disordered meso-macroporous materials. *Optic Express* **2014**, *22*, 7503−7513.

(11) Bachelard, N.; Gaikwad, P.; Backov, R.; Sebbah, P.; Vallée, R.A.L. Disorder as a Playground for the Coexistence of Optical Nonlinear Effects: Competition between Random Lasing and Stimulated Raman Scattering in Complex Porous Materials. *ACS Photonics* **2014**, *1*, 1206−1211.

(12) Gaikwad, P.; Bachelar, N.; Sebbah, P.; Backov, R.; Vallée, R.A.L. Competition and Coexistence of Raman and Random Lasing in Silica-Titania-Based Solid Foams. *Adv. Optical Mater.* **2015**, *3*, 1640c1651.

(13) Bernadet, S.; Tavernier, E.; Ta, D.-M. ; Vallée, R. A. L. ; Ravaine, S. ; Fécant A.; Backov, R. Bulk Photo-Driven CO_2 Conversion through TiO_2@Si(HIPE) Monolithic Macrocellular Foams. *Adv. Funct Mat.* **2019**, *29*, 1807767.

(14) Debecker, D. P.; Boissière, C.; Guillaume, L.; Huet, S.; Eliaers, P.; Sanchez, C.; Backov, R. First acidic macro-mesocellular aluminosilicate monolithic foams "SiAl(HIPE)" and their catalytic properties. *Chem. Commun.* **2015**, *51*, 14018−14021.

(15) Roucher, A.; Bentaleb, A.; Laurichesse, E.; Dourges, M.-A.; Emo, M.; Schmitt, V.; Blin, J.-L.; R. Backov, R. First Macro-Mesocellular Silica SBA-15-Si(HIPE) Monoliths: Conditions for Obtaining Self-Standing Materials. *Chem. Mater*. **2018**, *30*, 864−873.

(16) Roucher, A.; Emo, M.; Vibert, F.; Stébé, M-J.; Schmitt, V.; Jonas, F.; Backov, R.; Blin, J-L. Investigation of mixed ionic/nonionic building blocks for the dual templating of macro-mesoporous silica foams. *J. Coll. Inter. Sci.* **2019**, *533*, 385−400.

(17) Royer, S.; Duprez, D. Catalytic Oxidation of Carbon Monoxide over Transition Metal Oxides *Chem. Cat. Chem*. **2011**, *3*, 24–65.

(18) Wang, R.; He, H.; Wang, J.; Liu, L.; Dai, H. Shape-regulation: An effective way to control CO oxidation activity over noble metal catalysts. *Catal. Today* **2013**, *201*, 68–78.

(19) Kamiuchi, N.; Haneda, M.; Ozawa, M. CO oxidation over Pt/Ce–Zr oxide catalysts with low content of platinum and cerium components. *Catal. Today* **2013**, *201*, 79–84.

(20) Han, W.; Zhang, P.; Tang, Z.; Lu, G. Low temperature CO oxidation over Pd–Ce catalysts supported on ZSM-5 zeolites. *Process Saf. Environ. Prot.* **2014**, *92*, 822–827.

(21) Salomons, S.; Hayes, R.E.; Votsmeier, M.; Drochner, A.; Vogel, H.; Malmberg, S.; Gieshoff, *J.* On the use of mechanistic CO oxidations models with a platinum monolith catalyst. *Appl. Catal. B Environ*. **2007**, *70*, 305–313.

(22) Fuchs, S.; Hahn, T.; Lintz, H.-G. The oxidation of carbon monoxide by oxygen over platinum, palladium and rhodium catalysts from 10^{-10} to 1 bar. *Chem. Eng. Process. Process Intensif.* **1994**, *33*, 363–369.

(23) Figueroa, S.J.A.; Newton, M. A. What drives spontaneous oscillations during CO oxidation using O_2 over supported Rh/Al_2O_3 catalysts? *J. Catal.* **2014**, *312*, 69–77.

(24) Alonso, E.; Field, F. R.; Kirchain, R. E. Platinum Availability for Future Automotive Technologies *Environ. Sci. Technol.* **2012**, 46, 12986–12993.

(25) Liu, W.; Flytzani-Stephanopoulos, M. Transition metal-promoted oxidation catalysis by fluorite oxides: A study of CO oxidation over Cu/CeO_2. *Chem. Eng. J.* **1996**, *64*, 283–294.

(26) Biabani-Ravandi, A.; Rezaei, M.; Fattah, Z. Study of Fe-Co mixed metal oxide nanoparticles in the catalytic low-temperature CO oxidation. *Process Saf. Environ. Prot*. **2013**, *91*, 489–494.

(27) Lukiyanchuk, I. V.; Rudnev, V.S.; Chernykh, I. V.; Malyshev, I. V.; Tyrina, L.M.; Adigamova, M. V. Composites with transition metal oxides on aluminum and titanium and their activity in CO oxidation. *Surf. Coat. Technol*. **2013**, *231*, 433–438.

(28) Kang, M.; Song, M. W.; Lee, C.H. Catalytic carbon monoxide oxidation over CoO_x/CeO_2 composite catalysts. *Appl. Catal. A Gen.* **2003**, *251*, 143–156.

(29) Lin, H.; Chiu, H.; Tsai, H.; Chien, S.; Wang, C. *Catal. Lett.* **2003**, *88*, 169–174.

(30) Song, W.; Poyraz, A. S.; Meng, Y.; Ren, Z.; Chen, S.-Y.; Suib, S. L. Mesoporous Co_3O_4 with Controlled Porosity: Inverse Micelle Synthesis and High-Performance Catalytic CO Oxidation at −60 °C. *Chem. Mater*. **2014**, *26*, 4629–4639.

(31) Lou, Y.; Ma, J.; Cao, X.; Wang, L.; Dai, Q.; Zhao, Z.; Cai, Y.; Zhan, W.; Guo, Y.; Hu, P.; Lu, G.; Guo, Y. Promoting Effects of In_2O_3 on Co_3O_4 for CO Oxidation: Tuning O_2 Activation and CO Adsorption Strength Simultaneously. *ACS Catal.* **2014**, *4*, 4143–4152.

(32) Brunauer, S.; Emmett, P. H.; Teller, E. Adsorption of Gases in Multimolecular Layers. *J. Am. Chem. Soc.* **1938**, *60*, 309–319.

(33) Carretero-Genevrier, A.; M. Gich, M.; L. Picas, L.; Gazquez, J.; Drisko, G.L.; Boissiere, C.; D. Grosso, Rodriguez-Carvajal, J.; Sanchez, C. Soft-Chemistry–Based Routes to Epitaxial α-Quartz Thin Films with Tunable Textures. *Sciences*, **2013**, *340*, 827–831.

(34) Zangi, R. Can Salting-in/Salting-out Ions Be Classified as Chaotropes/Kosmotropes? *J. Phys. Chem. B,* **2010**, *114*, 643–650.

(35) Poyraz, A.S.; Dag, Ö. Role of Organic and Inorganic Additives on the Assembly of CTAB-P123 and the Morphology of Mesoporous Silica Particles. *J. Phys. Chem. C*. **2009**, *113*, 18596–18607.

(36) Brinker, C.J.; Scherer, G. W. Sol-Gel Science *in* "*The Physics and Chemistry of Sol-Gel Processing", Academic Press*, **1990,** 1–912.

(37) G. Porod, G. in "*Small Angle X-ray Scattering*", Glatter, O.; Kratky, O. Academic Press, London, **1982,** Chap. 2, 17–51.

(38) Lisboa-Filho, P.N.; de Almeida, M.R.C.; Gallo, P.L.; Azevedo,E.; Paskocimas, C.A.; Longo, E.; Ortiz, W.A. Magnetic phases of imperfectly crystalline Co_2SiO_4. *Journal of Non-Crystalline Solids* **2000**, *273*, 277–281.

(39) Nguyen, P.Q.H; Zhang, D.; Rapp, R.; Bradleya, J.P.; Dera P. Room temperature facile synthesis of olivine-Co_2SiO_4 nanoparticles utilizing a mechanochemical method. *RSC Adv*, **2021**, *11*, 20687–20690.

(40) Takada, T.; Bando, Y.; Kiyama, M.; Miyamoto H.; Sato, T. The Magnetic Property of β-$Co(OH)_2$. *J. Phys. Soc. Jpn.* **1966**, *21*, 2726–2726.

(41) Carlin, R.L. *in "Magnetochemistry", Springer Ed.*, Berlin, **1986,** 1-328.

(42) Li, H.B.; Liu, P.; Liang, Y.; Xiao, J.; Yang, G.W. Amorphous cobalt hydroxide nanostructures and magnetism from green electrochemistry. *RSC Adv.*, **2013**, *3*, 26412–26417.

(43) Dutta, P.; Seehra, M.S.; Thota, S.; Kumar, J. A comparative study of the magnetic properties of bulk and nanocrystalline Co_3O_4. *J. Phys.: Condens. Matter* **2007**, *20*, 015218.

(44) Taylor, S.H.; Hutchings, G.J.; Mirzaei, A.A. Copper zinc oxide catalysts for ambient temperature carbon monoxide oxidation. *Chem. Commun*. **1999**, *15*, 1373–1374.

(45) Pillai, U.R.; Deevi, S. Room temperature oxidation of carbon monoxide over copper oxide catalyst. *Appl. Catal. B Environ.* **2006**, *64*, 146–151.

(46) Lou, Y.; Wang, L.; Zhao, Z.; Zhang, Y.; Zhang, Z.; Lu, G.; Guo, Y.; Guo, Y. Low-temperature CO oxidation over Co_3O_4-based catalysts: significant promoting effect of Bi_2O_3 on Co_3O_4 catalyst. *Appl. Catal. B Environ*. **2014**, *146*, 43–49.

(47) Lablokov, V.; Barbosa, R.; Pollefeyt, G.; Van Driessche, I.; Chenakin, S.; Kruse, N. Catalytic CO Oxidation over Well-Defined Cobalt Oxide Nanoparticles: Size-Reactivity Correlation. *ACS Catal*. **2015**, *5*, 5714–5718.

(48) Lima, T.M.; Castelblanco, W.N.; Rodrigues, A.D.; Roncolatto, R.E.; Martins, L.; Urquieta-González, E.A. CO oxidation over Co-catalysts supported on silica-titania–The

effects of the catalyst preparation method and the amount of incorporated Ti on the formation of more active Co^{3+}species. *Appl. Catal. A Gen.* **2018**, *565*, 152–162.

(49) Kuboňová, L.; Peikertová, P.; Kutláková, K.M.; Jirátová, K.; Slowik, G.; Obalová, L.; Cool, P. Catalytic activity of cobalt grafted on ordered mesoporous silica materials in N_2O decomposition and CO oxidation. *Mol. Catal*. **2017**, *437*, 57–72.

(50) Prasad, N.R.; Singh, S. V. Catalytic abatement of CO, HCs and soot emissions over spinel-based catalysts from diesel engines: An overview. *J. Environ. Chem. Eng.* **2020**, *8*, 103627.

(51) Wang, C.B.; Tang, C.H.; Tsai, H.C.; Chien, S.H. Characterization and Catalytic Oxidation of Carbon Monoxide over Supported Cobalt Catalysts. *Catal. Lett.* **2006**, *107*, 223–230.

(52) Dey, S.; Dhal, G.C. The catalytic activity of cobalt nanoparticles for low-temperature oxidation of carbon monoxide. *Mat. Today Chem.* **2019**, *14*, 100198.

(53) Rosynek, M.P.; Polansky, C.A. Effect of cobalt source on the reduction properties of silica-supported cobalt catalysts. *Appl. Catal*. *A* **1991**, *73*, 97–112.

(54) Jacobs, G.; Chaney, J.A.; Patterson, P.M.; Das, T.K.; Davis, B.H. Fischer–Tropsch synthesis: study of the promotion of Re on the reduction property of Co/Al_2O_3 catalysts by in situ EXAFS/XANES of Co K and Re L_{III} edges and XPS. *Appl. Catal. A* **2004**, *264*, 203–212.

(55) Eschermann, T.O.; Oenema, J.; de Jong, K.P. Effects of noble metal promotion for Co/TiO_2 Fischer-Tropsch catalysts. *Catal. Today* **2016**, *261*, 60–66.

(56) Backov, R. Combining soft matter and soft chemistry: integrative chemistry towards designing novel and complex multiscale architectures. *Soft Matter*. **2006**, *2*, 452–464.

TOC

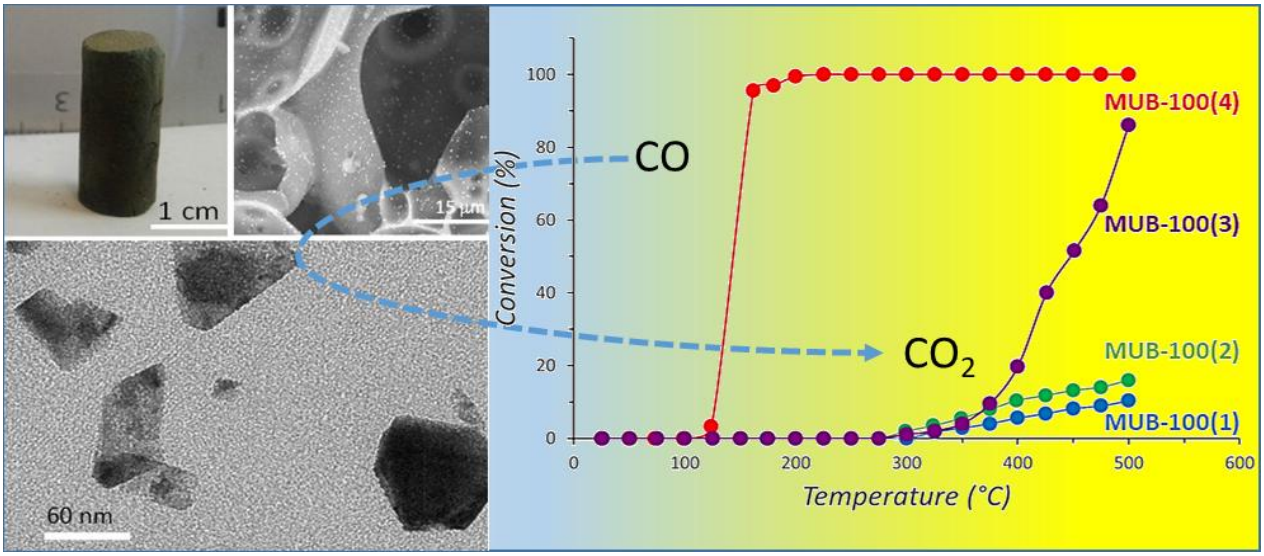
1 cm
15 µm
60 nm
CO
CO_2
Conversion (%)
Temperature (°C)
MUB-100(4)
MUB-100(3)
MUB-100(2)
MUB-100(1)
0
20
40
60
80
100
0
100
200
300
400
500
600